

Microstructure and Mechanical Properties of 21-6-9 Stainless Steel Electron Beam Welds

J. W. Elmer, G. F. Ellsworth, J. N. Florando, I. V. Golosker, R. P. Mulay

February 5, 2016

Integrating Materials and Manufacturing Innovation

Disclaimer

This document was prepared as an account of work sponsored by an agency of the United States government. Neither the United States government nor Lawrence Livermore National Security, LLC, nor any of their employees makes any warranty, expressed or implied, or assumes any legal liability or responsibility for the accuracy, completeness, or usefulness of any information, apparatus, product, or process disclosed, or represents that its use would not infringe privately owned rights. Reference herein to any specific commercial product, process, or service by trade name, trademark, manufacturer, or otherwise does not necessarily constitute or imply its endorsement, recommendation, or favoring by the United States government or Lawrence Livermore National Security, LLC. The views and opinions of authors expressed herein do not necessarily state or reflect those of the United States government or Lawrence Livermore National Security, LLC, and shall not be used for advertising or product endorsement purposes.

Mechanical Properties of 21-6-9 Stainless Steel Electron Beam Welds

by:

John W. Elmer^{1*}, G. Fred Ellsworth¹, Jeff N. Florando¹, Ilya V. Golosker¹, and Rupalee Mulay¹

Keywords

Electron Beam Welding, Stainless Steel, Nanoindentation, Quasi-static Strain Rate, Cross-Weld Tensile Testing, Hardness, Weld Strength Modeling

Abstract

Welds can either be stronger or weaker than the base metals that they join depending on the microstructures that form in the fusion and heat affected zones of the weld. In this paper, weld strengthening in the fusion zone of annealed 21-6-9 stainless steel is investigated using cross-weld tensile samples, hardness testing, and microstructural characterization. Due to the stronger nature of the weld, the cross-weld tensile tests fail in the base metal and were not able to generate true fusion zone mechanical properties. Nanoindentation with a spherical indenter was instead used to predict the tensile behavior for the weld. Extrapolation of the nanoindentation results to high strains was performed using the Steinberg-Guinan and Johnson-Cook strength methods, and the results can be used for weld strength modeling purposes. The results illustrate how microstructural refinement in the weld fusion zone can be an effective strengthener for 21-6-9 stainless steel.

^{*} Corresponding Author

Data Description

Introduction

Electron beam (EB) welds in annealed 21-6-9 stainless steel (SS) sheet were made and characterized to determine the weld fusion zone (FZ) and base metal mechanical properties for use in structural design calculations. Alloy 21-6-9 SS, also known as Nitronic 40, was developed as an improved austenitic stainless steel over traditional 300 series stainless steel alloys. This alloy contains nominally 21%Cr, 6%Ni, 9% Mn, and has improved corrosion resistance due to its higher Cr content of 21%. In addition, 21-6-9 SS uses N rather than C as a strengthener, which reduces the tendency for corrosion sensitization that can occur during heat treating and welding. Nitrogen can be added up to 0.35%, which improves the room temperature yield strength of 21-6-9 SS over 300 series stainless steel alloys, while maintaining good toughness and high ductility (>40%). Manganese is added to 21-6-9 SS to increase austenite stability, particularly at cryogenic temperatures, while reducing the Ni content from 8% to 6% as compared to 300 series stainless steels. 21-6-9 SS can be further strengthened by cold work and can be machined, forged, and welded using the same methods as 300-series stainless steels. A review report on characterization of 21-6-9 SS base metal can be found in [1], and its yield stress over a wide range of strain rates and temperatures can be found in [2].

Although the base metal properties of 21-6-9 SS are well documented, the properties of the welds are not as well understood. Measuring the mechanical properties of weld joints is complicated by the fact that microstructure and property gradients are formed in the weld FZ and heat affected zone (HAZ) of the weld due to the localized nature of welding heat sources. Oftentimes, the welds are not large enough to allow the extraction of all weld metal tensile bars from the FZ, and under these circumstances cross-weld tensile bars are sometimes used. The cross-weld tensile samples give an overall measure of the joint performance and fail in the weakest portion of the weld region, which may be the base metal, HAZ or FZ depending on the material and the welding conditions. In order to measure the mechanical properties of the weld FZ itself, hardness measurements are often performed and sometimes correlated with stress-strain behavior using micro- and nano- indentation methods [3, 4].

This study characterizes EB welds tested in a cross-weld geometry with different sample sizes and configurations, and the results are compared to a nanoindentation method for predicting stress-strain behavior. The results are modeled using Steinberg-Guinan and Johnson-Cook methods to create mechanical property data for 21-6-9 SS welds over a wide range of strains under quasi-static conditions at room temperature.

Material and Experimental Procedures

Materials

Annealed 21-6-9 SS plate was acquired with the composition summarized in Table 1, where the measured "actual" composition of this plate is compared to the commercial "specification and the desired "Aim" composition range for weldability. The Aim alloy composition has a lowered nitrogen content compared to the standard specification to improve electron beam weldability. The initial plate measured 3 mm thick and was further machined to the size of $100 \times 200 \times 1.5$ mm for welding and mechanical property testing. Ferrite measurements were made on the base metal using a Magne-Gage tester and a number 3 magnet, showing that the base metal had no measurable ferrite. After welding, the ferrite content was measured on polished cross sections and on the top of the electron beam weld beads, showing that the welds contained delta ferrite that measured between 0.8 to 1.1%. However, due to the small weld volume (~1 mm deep, 1.5 mm wide), the magnetic measurements underestimate the actual ferrite content of the weld by as much as 5X due to incorporation of the zero percent base metal ferrite into the readings [5].

Electron Beam Welding

Samples to be welded were machined to the size of 50 x 200 x 1.5 mm, so that when welded along their length they would have the same dimensions as the base metal samples. The weld joint preparation was a step joint configuration, which has a step height requiring 1 mm weld penetration. Electron beam welds were made using LLNL electron beam welder Hamilton Standard 605. All welds were made with a 9 inch work distance, and performed at 4x10⁻⁵ torr vacuum. The Enhanced Modified Faraday Cup (EMFC) electron beam diagnostic was used to measure the properties (peak power density, full width half maximum, beam diameter, and beam aspect ratio) of each beam prior to welding using the method detailed elsewhere [6].

Tensile Testing

The base metal and welded plates were electro discharge machined (EDM) into two different sized tensile bars as illustrated in Figure 1. The "standard " tensile bars measured 4 inch long, and are based on an ASTM E-8 tensile sample with a length-to width ratio of 4:1. The "mini" tensile samples were 2/5 size and maintained the same 4:1 length to width ratio. Tensile bars removed from the welded plate are cross-weld tensile samples, since all-weld, longitudinal, tensile bars were not able to be prepared due to the small volume of welded material. The welded tensile samples were further prepared using two methods as illustrated in Fig. 2. The first method used the tensile bar in the full-thickness (1.5 mm) as welded condition, i.e., with an unwelded portion of joint directly below the step joint. The second method prepared the welds

by machining the top and bottom surfaces of the welded sample to a final thickness of 0.75 mm so as to remove any weld reinforcement and undercut on the top surface and the unwelded portion below the step. Cross sectional areas of the samples were measured, to calculate the stress, on each sample to account for any variations in machining that may have occurred.

The "mini" sample tests were performed in an Instron 4444 electromechanical test machine at room temperature and position control at a rate of 0.020 in/min. A strain extensometer with a gage length of 0.225 inch – 50% was used to measure strain for the base and milled weld minitensile samples, while a 0.138 inch gage length was used on the full thickness mini samples. In all cases the knife edges of the extensometer were located across the width of the sample and centered over the weld. The "standard sample" tests were performed in an Instron 5800R/4505 test machine at room temperature and position control at a rate of 0.050 in/min. An EIR LE-01 laser extensometer with a 1 inch gage length was used to measure strain for the standard sized samples, with the gage length centered over the weld, and with the laser facing the top (weld side) of the sample. The laser measured the extension of two dimples on the sample that defined the gage length. The modulus of elasticity was determined by the best fit straight line through the linear portion of the stress-strain curve, the yield strength was determined using a 0.2% offset method, and the ultimate tensile strength was determine by the peak load divided by the load bearing area at the thinnest portion of the step joint sample configuration.

Microstructure, Microhardness, and Nanoindentation Testing

Metallographic cross sections of the welds and base metals were performed using standard preparation procedures. The samples were sectioned on a slow speed diamond saw, potted in a clear two-part epoxy, and then ground on successive silicon carbide papers from 320 to 2400 grit. The samples were polished first using 3 micron diamond paste, followed by a 1 micron alumina slurry. The samples to be etched were electrolytically etched in a 5-10% oxalic acid solution at room temperature to bring out the microstructure. Macrophotographs of the entire weld fusion zone shapes were made using a Keyence VHX-600E Digital Microscope, while higher magnification micrographs were made using a Reichert inverted stage metallograph.

SEM imaging in the backscattered mode and electron backscattered diffraction (EBSD) was carried out on a Philips FEG XL 30S SEM with a field emission gun. The SEM is equipped with an EBSD camera and a TSL data acquisition system. Step size increments of 2 micron were used to image the grain structure in the entire weld fusion zone, and step size increments as small as 0.1 micron were used to zoom in on individual fusion zone grains.

Vickers microhardness testing was performed on a calibrated Leco AMH43 microhardness testing system with load range from 1 to 500 gm. The indentations were made using a 50 gm load, and were manually measured using a 50x objective to determine the Vickers Hardness indentation diagonal lengths, which were typically about 20 microns corner to corner.

Nanoindentation hardness testing was done using a spherical indenter to measure load-depth curves that could be converted into approximate stress-strain material behavior. This method was particularly useful for estimating the stress-strain behavior of the welds, since the fusion zones were too small for a standard tensile test method. The 21-6-9 SS samples (polished, but not etched, base and weld metal) were testing in the B231 G200 Nanoindenter from Agilent. A 50 micron radius spherical diamond tip was used during these tests. The advantages of this nanoindenter are that it has high load and displacement resolution, on the order of 50 nN and 1 nm respectively, and with the high load option can go up to 10 N of force. Due to the relatively large diameter of the sphere coupled with the high strength of 21-6-9 SS, the high load option was used for these tests. In addition, this nanoindenter can apply an oscillating signal on top of the load signal which permits the stiffness of the material to be measured continuously (CSM) as a function of depth. All the tests were run using the high load and CSM options to measure the stiffness which is used in the calculation of stress and strain.

Electron Beam Welds and Microstructure

Electron beam welds were made using 110 kV, 5.5 mA (605 W) at a weld speed of 60 ipm, with a +30 mA defocused. This beam was characterized with the Enhanced Modified Faraday Cup and shown to have a peak power density (PPD) of 1.5-1.6 kW/mm², a beam diameter ($1/e^2$) of 0.90-1.0 mm, and a beam full width half maximum (FWHM) of 0.50-0.55 mm. A representative power density distribution for this weld is shown in Fig. 3. Note that the beam is not circular at this level of defocus, and has an elliptical shape with an aspect ratio of approximately 1.8:1. A typical cross section through the resulting weld is shown in Fig. 2a, and a summary of the EB welding parameters, weld penetrations, and weld widths is presented in Table 2 from cross-sections taken from 6 welds. The weld penetrations varied from 0.98 to 1.14 mm, while the weld widths across the top surface varied from 1.51 to 1.56 mm. Undercutting appears on one side of the top surface that measures 52.7 \pm 5.4 μ m. The maximum undercut was measured to be 58 μ m, leaving at least 0.800 mm of full weld fusion zone above the step for removal of the 0.750 mm thick milled tensile samples.

At high magnifications, the 21-6-9 SS weld microstructure was shown to be considerably different than the base metal microstructure. Fig. 4a shows the base metal microstructure which has consists of equiaxed grains that have an average grain diameter of approximately 50

μm. Annealing twins are present in many of the grains, and small inclusions are randomly dispersed. The base metal microstructure is banded due to the effects of chemical segregation during ingot casting and subsequent hot working and rolling. The chemical segregation is typical of 21-6-9 SS plate. No delta ferrite was observed or measured in the base metal portions of the samples. The weld microstructure is shown at the fusion boundary in Fig. 4b and in the central portion of the fusion zone in Fig. 4c. The microstructure consists of austenite (light etching phase) with some remnant delta ferrite (dark etching phase). The majority of the microstructure appears to have formed by the solidification of primary ferrite with second phase austenite (FA) mode where the primary ferrite dendrites that form during solidification partially transform to austenite during cooling [7]. The remaining vermicular/skeletal ferrite is concentrated at the original cores of the ferrite dendrites, and represents only a small fraction of the original primary ferrite phase that formed.

Figure 5a shows a higher magnification micrograph of the fusion boundary, where the remaining ferrite can be seen more clearly, and represents about 3-5% of the fusion zone microstructure in this location. Epitaxial regrowth of austenite from the base metal (1-2 μ m) is followed by a zone (~10 μ m) that is difficult to interpret and initially may be the AF solidification mode, which then transitions to the primary ferrite (FA) mode of solidification deeper into the fusion zone. Also note the grain boundary ferrite that formed near the heat affected zone (HAZ) at the upper left portion of the fusion zone. Figure 5b shows a higher magnification micrograph near the center of the fusion zone, which clearly solidified in the FA mode with skeletal ferrite present throughout the majority of the microstructure, and lacy ferrite [7] present in the upper right hand side of the micrograph. The ferrite content appears to vary between about 5% and 15% depending on the local ferrite morphology. The higher amount of ferrite observed in the microstructure relative to that measured by the Magne-gage (~1%) is related to the inherent error of measuring ferrite with the Magne-gage on small weld samples that incorporate base metal (0% ferrite) into the reading.

Figure 6a shows the EBSD results on a 001 inverse pole figure from a cross section of one of the welds, including the base metal grains. The annealed base metal has a random grain orientation with apparent annealing twins in many of the grains. The weld has a columnar macrostructure with elongated grains forming in a pattern that follows the heat flow direction from the fusion zone boundary to the top center of the weld. In Fig. 6a, a large EBSD step size of 2 micron was used to map the entire weld, and at this resolution, the grains in the fusion zone all index as FCC austenite, indicating that the weld contains only a small amount of BCC residual ferrite. A higher resolution EBSD image taken inside the fusion zone is shown in Fig. 6b, which was acquired with a 0.1 micron step size. In this image, the FCC grains are indexed, but the residual ferrite is not clearly identified due to the small size of the residual dendrite cores that are less than 1 micron wide. The important information from these images is that,

although there is a columnar nature to the growth of the predominantly austenite phase in the weld fusion zone, the grain orientations are randomly oriented in the cross section of the weld.

Mechanical Properties of the Base Metal and Welds

Table 3 summarizes the microhardness measurements that were made on the base metal, the electron beam fusion zone, and the HAZ for each of the 6 welded coupons. A total of 36 hardness measurements were made on the base metal samples, showing that the base metal had an average hardness of 212.1 ± 10.9 HV. These values correspond to annealed 21-6-9 SS sheet, which has a handbook value of RB 94 (HV 213) [8]. After welding, the fusion zone hardness was measured at 254.4 ± 9.7 HV based on 62 measurements made in the 6 welds. These results show a 20% increase in hardness after welding relative to the 21-6-9 SS base metal, due to the fine two-phase weld solidification structure as described above.

Additional microhardness measurements were made in the HAZ of the welds by placing the indenter in the base metal at a distance of 1-2 indentation distances (20-40 micron) from the weld fusion line. The resulting measurements showed HAZ hardness values midway between the weld fusion zone and the base metal of 232.1 ± 13.9 HV. The apparent strengthening of the HAZ is more likely due to the indentation being artificially affected by the nearby harder weld metal than an actual increase in hardness of the HAZ, based on the belief that there should be no HAZ hardening mechanisms in the annealed 21-6-9 SS heat affected zone.

Stress-Strain Behavior of Cross-Weld Tensile and Base Metal Samples

The base metal and two different types of cross-weld samples were tensile tested to failure in both standard (4 inch long) and mini (1 inch long) configuration dog-bone shaped samples. Figure 7 shows the failure behavior for each of the six different tensile bar configurations. The base metal samples for the mini (a) and standard (d) tensile configurations failed approximately in the middle of the gage length with necking occurring mostly through the thickness of the bars. The welded samples that were milled to remove the effects of the unwelded step and weld reinforcement for the mini (b) and standard (e) tensile configurations failed approximately half-way between the weld and the radius that forms the tensile grips. In both cases a "lump" of weld metal is left behind where the stronger weld fusion zone deforms less than the base metal away from the weld. The final failures have a similar necking appearance to the base metal samples. The welded samples that were pulled in the full-thickness, as received, condition for the mini (c) and standard (f) tensile configurations failed in a completely different manner. Due to the reduced amount of load bearing material above the step, the samples

failed in the base metal close to the weld, tearing through the base metal and HAZ with less apparent necking and less measured strain to failure than the other samples.

Figure 8 shows close up photos of the necked regions of the broken mini tensile samples. The base metal sample is shown in (a) and (b) for the side and top views of the fractured sample respectively. Thinning of the sample through the thickness and across the width of the sample is apparent. The failure is ductile in appearance, and final failure occurred with the formation of a shear lip at approximately 45 degrees to the tensile axis. The milled cross-welded sample is shown in (c) and (d) for the side and top views of the fractured sample respectively. The weld location is marked in the figures and it is clear that the fracture occurred well away from the weld. It can also be seen that the weld region deformed less than the base metal, being wider and thicker than the adjacent base metal. Just like the base metal sample, the failure is in the base metal and the final failure occurred with the formation of a shear lip at approximately 45 degrees to the tensile axis. The full-thickness, as welded, cross-weld sample is shown in (e) and (f) for the side and top views of the fractured sample respectively. The cross section shows that the location of the failure is clearly adjacent to the fusion line of the weld in the reduced thickness portion of the sample. As before the final failure is ductile in appearance, forming a 45 degrees shear lip relative to the tensile axis. Some localized deformation extends from the base of the weld and appears to follow a columnar weld grain boundary into the weld fusion zone. The top view of the failed sample shows narrowing occurring on the side of the weld with the reduced section thickness, and little to no narrowing on the thick section side of the weld.

This same as-welded tensile sample was then polished and etched to show the deformation and failure locations more clearly. Figure 9a shows the sample lightly polished and etched, indicating that the weld region above the step is deforming, while the remainder of the weld appears comparatively unstrained. Figure 9b shows the same sample after lapping more deeply below the surface and then repolishing and etching, showing that the final failure occurred in the base metal adjacent to the fusion zone. A high magnification photo of the failed region adjacent to the fusion line is shown in Fig. 9c. The individual base metal grains near the fusion line contain wavy deformation bands. These bands are likely the result of strain-induced martensite, which forms during deformation and is known to be the principal strain hardening mechanism in stainless steels [9], and is also known to form in 21-6-9 SS at high strain rates [10]. Microhardness measurements made in necked region of the failed sample showed that the hardness is 394.8+12.0 HV for 9 data points, which is considerably harder than the undeformed base metal (212.2 HV) or the weld (254.4 HV).

Figure 11 plots the uniaxial engineering stress versus engineering strain tensile behavior of the base metal samples for both the mini and standard tensile configurations, and the resulting data are summarized in Table 4. The base metal tensile samples showed yield stresses (σ_y) that

varied from 50.0 to 53.0 ksi, with the mini tensile bars having yield strengths on the lower end of this range. All curves show significant strain hardening with ultimate tensile strengths (UTS) varying between 101.6 to 104.4 ksi, with the mini tensile bars on the upper end of this range. The elongations at failure varied from 47% to 62% for the base metal samples using the laser extensometer with the 1 inch gage length. The mini samples, with the smaller 0.225 inch gage length, showed high elongations, up to 80%. Note that the extensometer was removed prior to failure of the mini samples, resulting in the small load drop observed in the plotted curves. The subsequent stress-strain behavior after the extensometer was removed was estimated from the load versus crosshead displacement measurements, which is an approximation that doesn't match the strain hardening rate measured by the extensometer.

Figure 11 plots the results plots as engineering stress versus engineering strain curves for the milled weld samples. These samples behaved nearly identically to the base metal samples with yield strengths varying from 52.8 to 55.7 ksi, and ultimate strengths varying from 103.9 ksi to 105.8 ksi as summarized in Table 4. The elongations to failure for the standard sized samples were similar to those of the base metal, varying from 54% to 63%, while those for the mini samples again displayed slightly higher elongations at failure. Observations of the tensile samples showed that in all cases, the milled cross-weld tensile samples failed in the base metal due to the higher strength of the weld. Because of this, the yield and ultimate strengths measured on these samples essentially match those of the base metal samples, showing that this sample configuration is not good for measuring the true weld fusion zone properties.

Figure 12a plots the engineering stress versus engineering strain results of the full thickness, as welded, samples. In this configuration, the weld reinforcement and unwelded portion of the step were not removed, as illustrated in Fig. 12b. The tensile behavior is quite different than for the milled cross-weld tensile samples. Yield strengths, based on the area of the sample above the weld step, were considerably higher than the other samples with values up to 76.3 ksi for the standard samples, and values up to 75.5 ksi for the mini samples. These strengths are 25-43% higher than in the other two sample configurations. The difference in behavior can be explained with the aid of Fig. 12b that schematically illustrates the full thickness test sample. In these as welded samples, there is a region of reduced area, and thus high stress concentration, directly above the unwelded step, which contains a large fraction of welded metal. The higher yield strengths measured on the full thickness samples are partly based on the fact that the high strain region contains some fraction of higher strength welded metal. However, strain localization above the weld step id more likely the larger factor in contributing to the measured increased yield strength of the as cross weld samples. The elongations were also different than the milled cross-weld samples. The standard sized full-thickness cross-weld samples all failed with total elongations of only 10%, while the mini samples failed between 22% and 27% elongation. The reduced elongations are also likely to be the direct result of the

strain localization above the weld step, and the fact that the extensometers span a much wider area than the highly strained region. Peak loads were used to calculate the UTS based on the reduced cross sectional area of the sample above the unwelded portion of the step, showing values between 102.3 and 110.2 ksi, which are similar to the tensile tests in the other sample geometries. Note that the measured modulus data for the full thickness samples was not accurate due to the change in section thickness and bending of the samples. This effect is magnified with the shorter gage length mini sample where a larger fraction of necking is present in the gage length.

In summary, the tensile test results show that the cross-weld samples failed in the base metal portions of the tensile bar, and produced strengths comparable to the all base metal samples having a 0.2% offset yield strength of 53.1±1.9 ksi, an ultimate strength of 105.3±2.2 ksi, and a Young's modulus of 29.4±0.95 Msi. The engineering strain at failure measured on the standard sized samples with a 1 inch gage length was approximately 60%, while the mini samples for both the base metal and the milled cross-weld configurations, had higher measured elongations due to the larger fraction of necked region in the 0.225 inch gage length. The full-thickness cross-weld tensile samples, are representative of the real weld, and showed highly localized strain behavior in the reduced thickness portion of the step welded joint. The associated change in thickness near the cross-tensile weld resulted in a reduced engineering strain at failure, higher yield strengths (73.4±3.9 ksi), and similar UTS measurements as the other tensile test samples and configurations. Based on these results, other methods are required to determine the mechanical properties of the weld FZ since none of the cross-weld sample configurations produced representative weld FZ properties.

Nanoindentation Estimation of the Stress-Strain Behavior of the Welds

An alternate method that can be used to measure the stress-strain behavior of small welds relies on an indentation technique. During indentation, the hardness of a material, defined as the load/area, is measured. The stress state during indentation however is much more complicated than in a uniaxial test and can be influenced by the shape and material of the indenter [3]. During spherical indentation, the plastic zone develops gradually, allowing for the elastic-plastic transition to be probed in order to produce an indentation stress-strain curve. The spherical indentation method is used here to estimate the stress-strain behavior of the welded region of a 21-6-9 SS part, using the base metal, with known tensile behavior, for calibration.

The base metal and electron beam welded samples were metallographically prepared and indentation tested in the as-polished condition. The loading rate was 50 nm/s for each indent

to a depth of 7000 nm, which corresponds to a strain rate of about $1x10^{-4}/s$. These parameters were selected to match the strain rate of the standard tensile tests from the previous study, and reach a strain of about 10%. In order to convert the load, displacement, and stiffness data from the indentation test to indentation stress and strain, the following calculations were used, which follows the procedure [4]. The contact depth, h_c is calculated as:

$$h_C = h - 0.75 \frac{P}{S} \tag{1}$$

where h is the displacement, P is the load, and S is the contact stiffness, all which is taken directly from the nanoindenter. From the contact depth, the contact radius, a is

$$a = \sqrt{2h_c R_i - {h_c}^2} \tag{2}$$

where R_i is the radius of the indenter. The indentation strain, ε , is defined as:

$$\varepsilon = \frac{h_c}{2.4a} \tag{3}$$

And the indentation stress is:

$$\sigma_{ind} = \frac{P}{\pi a^2} \tag{4}$$

To relate the indentation stress to the uniaxial stress the Tabor relationship is used where

$$\sigma_{uniaxial} = \frac{\sigma_{ind}}{T} \tag{5}$$

where T is the Tabor factor that can be estimated by correlating the indentation load displacement curve with a known uniaxial stress-strain curve of the material.

For calibration, the samples were first indentation tested in the base metal and then compared with the uniaxial tension tests. The data from the spherical indentation test was then converted to an indentation stress and indentation strain using the procedure described above. The correlation factor (Tabor relationship), to relate the indentation stress to the equivalent uniaxial stress, was then determined by matching to the uniaxial tests. This correlation factor was then used in calculated the corresponding stress-strain data for the weld sample. The main assumption is that the correlation factor is roughly the same between the base metal and the welded 21-6-9 SS. In addition, estimates of the elastic modulus were determined from the CSM readings, showing that the base metal had a modulus of elasticity of 198.2± 1.62 MPa (six samples), and the weld had a modulus of elasticity of 190.1 ± 1.86 MPa (four samples). The

nanoindentation results for the base metal compare well with the modulus values measured here in uniaxial tension of 202.7±6.6 MPa (12 samples). However, the modulus of the weld measured by nanoindentation is statistically lower. The reason for the lower measured modulus of the weld is unclear at this point and will require additional analysis to determine if this is a real effect or an artifact of the nanoindentation test results.

Representative indenter-based stress-strain curves for the base metal are shown in Figure 13. In order to match the data, a Tabor factor of 3.6 was applied. The spherical indentation data shows an initial overshoot in the stress before comes back down to match the uniaxial data. This overshoot is most likely due to the fact that we are probing a smaller volume with the nanoindenter and therefore require a higher stress in the initial part before enough dislocations are generated to accommodate the strain. The analysis and Tabor factor was then used to create the indenter-based stress-strain data for the welded region, as shown in Fig. 14, and a comparison between the base metal and weld region is shown in Fig. 15. The yield stress for the weld region is clearly higher as a result of its refined microstructure. The strain hardening rate, however, is the same between the two types of materials, which suggests that the scale for the hardening mechanisms, such as dislocation interactions, are smaller than the grain size of the weld region.

To extrapolate the indentation data to larger strains, the Steinberg-Guinan model was used to fit the indentation data [11]. The Steinberg-Guinan relationship is defined as:

$$Y = Y_o [1 + \beta(\varepsilon + \varepsilon_i)]^n \frac{G(P, T)}{G_o} \le Y_{\text{max}}$$
 (6)

where Y_0 is the yield stress, β is the hardening coefficient, n is the hardening exponent, G_0 is the reference shear modulus, G(P,T) is temperature and pressure dependent shear modulus, and Y_{max} is the saturation stress representing the upper limit for the flow stress. For the experiments performed in this study the ratio of the shear moduli was assumed to be 1. Since the indentation stress-strain curve stops at around 10%, an additional data point was used to help constrain the fit. The additional data point is based on the Vickers microhardness results shown in Table 3, where the measured hardness for the base metal is 2.08 GPa [GPa=9.8*HV/1000] and for the weld metal is 2.49 GPa. Using the standard Tabor factor of 3.6 for a sharp Vickers indent, the flow stress at 8% strain should be around 590 MPa (85.7 ksi) for the base metal and 700 MPa (101 ksi) for the weld.

As a point of reference, there are published parameters for the Steinberg-Guinan model for 21-6-9 SS [12]. Since the published values are optimized for higher strain rates and Steinberg-Guinan is a rate independent model, it is expected that the published 21-6-9 SS parameters [12] would over predict the strength in comparison to the quasi-static experimental data. Figure 16

shows the over prediction of the stress-strain behavior for the published Steinberg-Guinan data when compared to one of the experimental uniaxial stress strain curves for the base metal from this study. Clearly, the Steinberg-Guinan published data need to be reevaluated for quasi-static strain rates. This was done by both fitting the base metal uniaxial stress-strain curves, and the nanoindentation results using the Material Implementation, Database, and Analysis Source (MIDAS) framework developed at Lawrence Livermore National Laboratory [13]. Fits were made out to 0.45 strain and passing through the appropriate points at 8% strain and are shown in Fig. 17. The same approach was used to fit and extrapolate the nanoindentation results for the electron beam welded material, and these results are plotted on Fig. 17 for comparison, showing the increased strength of the electron beam welds relative to the annealed 21-6-9 SS base metal. The Steinberg-Guinan model parameters for the base metal and weld are summarized and are compared to the published value [12] for 21-6-9 SS in Table 5.

An additional strength model that is commonly used is the Johnson-Cook strength relationship [14]. While also empirically based, there are additional terms which attempt to take into account the dependence on the strain rate and temperature, and the Johnson-Cook model has the following form:

$$Y = (A + B\varepsilon^{n})(1 + C \ln \frac{\dot{\varepsilon}}{\dot{\varepsilon}_{o}})(1 - T^{*_{m}}) + C_{p} p$$
(7)

and

$$T^* = \frac{T - T_{room}}{T_{melt} - T_{room}} \tag{8}$$

where, A is the effective yield stress at the reference strain rate, ϵ'_{o} (1/s) and temperature (T_{RT}), B is a strain hardening coefficient, n is the hardening exponent, C is the coefficient for the strain rate term, m is the exponential for the temperature dependence, and Cp is the pressure coefficient, and p is the actual pressure. The results of the Johnson-Cook model are compared to Steinberg-Guinan in Fig. 17, showing that both approaches can be used to represent the quasi-static uniaxial stress-strain behavior of 21-6-9 SS base metal and EB welds. The fitting parameters for Steinberg-Guinan and Johnson-Cook are summarized in Table 5 and Table 6 respectively.

In summary, spherical indentation with a nanoindenter can be used to measure the indentation stress strain behavior of 21-6-9 SS base metal and EB welds. The advantage for this technique is that the approximate stress-strain behavior can be measured using small amounts of material, such as welds. The main assumption in converting the indentation stress-strain behavior to uniaxial data is knowing the Tabor factor. For the 21-6-9 SS tested here, a Tabor factor of 3.6 was used, which matches the base metal indentation data to previous uniaxial

tests. In comparing the measured stress-strain behavior between the base metal and the weld region, the weld shows a higher yield stress, but the strain hardening rates are similar, suggesting similar hardening mechanisms.

Summary and Conclusions

Electron beam welding of annealed 21-6-9 stainless steel showed a significant hardening effect where the weld FZ is statistically harder than the annealed base metal. Metallographic characterization indicated that the weld solidified with a two-phase microstructure consisting of austenite plus 5-10% residual delta ferrite, as compared to 0% ferrite in the base metal. The primary mode of solidification was identified as ferrite with secondary austenite (FA), followed by solid state transformation of the majority of the ferrite to austenite during cooling. The resulting microstructure is skeletal ferrite with some lacy ferrite observed near the center of the weld. The higher hardness of the weld is due to the observed fine two-phase solidification microstructure relative to the equiaxed large grained austenitic base metal. Mechanical properties of the welds were further investigated using cross-weld tensile bars of different sizes and configurations and nanoindentation methods with a spherical indenter. From the results of these tests the following conclusions were made:

- 1. The 21-6-9 weld solidifies mainly in the primary ferrite mode (FA), followed by transformation of a majority of the ferrite to austenite. The resulting weld microstructure varies from about 5- 15% residual ferrite depending on the local ferrite morphology, as opposed to 0% ferrite in the annealed base metal. EBSD results confirm the majority phase as austenite, with a random grain orientation in the weld cross section, even though the weld fusion zone has a strong columnar nature with elongated grains following the heat flow direction.
- 2. Cross-weld tensile samples were not effective at measuring the mechanical behavior of the 21-6-9 stainless steel FZ metal since all failures occurred in the base metal regardless of tensile bar size or configuration. Results from the milled samples showed that the 0.2% offset yield stress (53.1±1.9 ksi), ultimate stress (105.3±2.3 ksi) and Young's modulus (29.4±0.95 Msi), were largely independent of sample size and are similar to the properties of the base metal samples. Elongations at failure varied from 47-62% in the standard sized milled samples with a 1 inch gage length, also similar to the base metal values.

- 3. The full thickness, as welded, cross-weld tensile samples did not match the results from the milled cross-weld samples or the base metal. The full thickness samples showed higher yield strengths than the milled samples of 73.4±3.9 ksi due to incorporation of stronger weld metal into the necked region near the final failure, and strain localization in this sample above the step in the weld. Other factors, such as the presence of a weld crown, sample bending, complicate the tensile behavior of the as welded samples. The measured elongations at failure were highly reduced in the as welded samples as compared to the other sample configurations at approximately 10% in the standard sized samples and 25% in the mini sized sample.
- 4. Microhardness measurements confirm weld strengthening in 21-6-9 SS. The weld metal was shown to have a statistically higher Vickers hardness HV of 254.4± 9.7, compared to the base metal hardness of 212.1± 10.9.
- 5. Nanoindentation using a spherical indenter was used to generate a stress-strain curve to about 10% strain for the 21-6-9 EB weld metal, as calibrated by the base metal tensile tests. A Tabor factor of 3.6 was determined to produce the best fit of the 21-6-9 SS base metal indentation curve to the uniaxial tensile test data. Results showed that the weld metal has a yield stress of 63.8 ksi, which is approximately 26% higher than that of the base metal 50.8 ksi.
- 6. Uniaxial stress-strain models were fit to the quasi-static experimental data in order to extend the nanoindentation weld results to higher strains. The Steinberg-Guinan and Johnson-Cook parameters for each model were determined for both the weld and base metals under quasi-static loading conditions as summarized in Table 5 and Table 6. It is notable that the published Steinberg-Guinan data for 21-6-9 SS produces yield strengths significantly higher than what is measured in uniaxial tensile experimental data at quasi-static strain rates. This difference is related to the fact that the Steinberg-Guinan published data are optimized for high strain rates [12].
- 7. The relative strength of the weld to the base metal is an important consideration for design when welded joints are present in the component. The results of the Steinberg-Guinan fit to the nanoindentation data under quasi-static strain rates indicate that the flow stress of the weld at 8% strain is 1.17x (101ksi/86 ksi) higher than that of the base metal.

Availability and Requirements of Software

MIDAS is an LLNL based software package that is currently not available outside LLNL, but a future version is being developed for general public use.

Availability of Supporting Data

Tabulated stress-strain data are available upon request.

List of Abbreviations

BCC-Body Centered Cubic

EB- electron beam

EDM- Electro-Discharge Machining

EMFC- Enhanced Modified Faraday Cup

FA-Primary Ferrite Solidification Mode

FCC-Face Centered Cubic

FWHM-Full Width at Half Maximum

FWe2- Beam Diameter at 1/e²

FZ-Fusion Zone

HV-Vicker's Hardness

HAZ-heat affected zone

JC- Johnson-Cook

MIDAS-Material Implementation, Database, and Analysis Source

PPD-Peak Power Density

SC- Steinberg-Guinan

SS- stainless steel

UTS-Ultimate Tensile Strength

Competing Interests

The authors declare that they have no competing interests.

Author's Contributions

JWE coordinated welding, microstructure characterization, tensile testing, and performed characterization of the electron weld beam. GFE provided program management guidance of the work performed. JNF performed MIDAS modeling of the tensile test results, and IVG performed nanoindentation hardness testing. RM performed EBSD characterization of the base metal and welds.

Author's Information

All authors work at Lawrence Livermore National Laboratory, Livermore, CA, 94550

- J. W. Elmer, elmer1@LLNL.gov, M/S L-342, phone 925 422-6543
- G. F. Ellsworth, ellsworth4@LLNL.gov, M/S L-125, phone 925 422-4622
- J. N. Florando, florando1@LLNL.gov, M/S L-342, phone 925 422-0698
- I. V. Golosker, golosker1@LLNL.gov, M/S L-342, phone 925 423-9166
- R. Mulay, mulay1@LLNL.gov, M/S L-342, phone 925 423-0412

Acknowledgment and Auspices

The authors would like to thank other LLNL employees who assisted with this work: Gilbert Gallegos for supplying the 21-6-9 SS material, Cheryl Evans for metallographic preparation and microhardness measurements, and Dave Hiromoto for tensile testing. This work was performed under the auspices of the U.S. Department of Energy by Lawrence Livermore National Laboratory under Contract DE-AC52-07NA27344. This document was prepared as an account of work sponsored by an agency of the United States government. Neither the United States government nor Lawrence Livermore National Security, LLC, nor any of their employees makes any warranty, expressed or implied, or assumes any legal liability or responsibility for the accuracy, completeness, or usefulness of any information, apparatus, product, or process disclosed, or represents that its use would not infringe privately owned rights. Reference herein to any specific commercial product, process, or service by trade name, trademark, manufacturer, or otherwise does not necessarily constitute or imply its endorsement, recommendation, or favoring by the United States government or Lawrence Livermore National Security, LLC. The views and opinions of authors expressed herein do not necessarily state or reflect those of the United States government or Lawrence Livermore National Security, LLC, and shall not be used for advertising or product endorsement purposes.

References

- 1. D. J. Alexander and C. T. Necker, "Characterization of Microstructures and Mechanical Properties of Current and Legacy 21-6-9 Stainless Steel Components" *Los Alamos National Laboratory Report, LA-UR-11-02857*, 2011.
- 2. M. E. Kassner and R. Breithaup, "The Yield Stress of Type 21-6-9 Stainless Steel Over a Wide range of Strain Rate (10⁻⁵ to 10⁴ s⁻¹) and Temperature," *LLNL Report, UCRL-89779*, 1983.
- 3. The Harndess of Metals, D. Tabor, 1951.
- 4. S.R. Kalidindi and S. Pathak, "Determination of the Effective Zero-Point and the Extraction of Spherical Nanoindentation Stress-Strain Curves," *Acta Met.*, V56, p3523, 2008.
- 5. J. W. Elmer, and T. W. Eagar, "Measuring the Residual Ferrite Content of Rapidly-Solidified Stainless Steel Alloys," Welding Journal 69 (4), p 141-s, 1990.
- 6. J. W. Elmer and A. T. Teruya, "An Enhanced Faraday Cup for the Rapid Determination of the Power Density Distribution in Electron Beams," *Welding Journal*, 80 (12), p 288s, 2001.
- 7. J. W. Elmer, S. M. Allen, and T. W. Eagar, "Microstructural Development During Solidification Of Stainless Steel Alloys," *Metall. Trans. A,* 20A (10), p 2117, 1989.
- 8. <u>Aerospace Structural Materials Handbook</u>, Vol 1 Ferrous Alloys, Battelle Columbus Division, 1987.
- 9. Handbook of Stainless Steels, Peckner and Bernstein, MGraw Hill, 1977.
- 10. C. Hills and H. Rack, "Effects of shock Deformation on the Residual Strength and Microstructure of Nitronic 40 Stainless Steel," *Mat. Sci. and Eng.*, 51, p. 231, 1981.
- 11. D. J. Steinberg et al, "A Constitutive Model for Metals Applicable at High Strain Rates," *JAP*, 51, p1499, 1980.
- 12. D. J. Steinberg, Equation of State and Strength Properties of Selected Materials, LLNL *UCRL-MA-106439*, February 13, 1991.
- 13. M. Tang, P. Norquist, N. Barton, K. Durrenberger J. Florando, A. Attia, MIDAS (Material Implementation, Database, and Analysis Source), *LLNL-PROC-464065*, December 2010.
- 14. G.R. Johnson and W.H. Cook, "A Constitutive Model and Data for Metals Subjected to Large Strains, High Strain Rates, and High Temperatures," *Proceedings of the 7th International Symposium on Ballistics*, The Hague, Netherlands, p 541, 1983.

Table 1: 21-6-9 stainless steel alloy composition compared to nominal and LLNL aim ranges.

Element	Actual	Specification	LLNL Aim
	(wt%)	(wt%)	(wt%)
Carbon	0.02	0.08 Max	0.04 max
Chromium	19.96	19.0-21.5	20-20.5
Nickel	7.02	5.5-7.5	6.0-6.5
Manganese	9.14	8.0-10.0	8.5-9.5
Silicon	0.05	1.0 Max	0.50 max
Nitrogen	0.23	0.15-0.40	0.23-0.25
Phosphorous	0.014	0.06 Max	0.000
Sulfur	<0.005	0.03 Max	0.000
Oxygen	<0.001		0.000-0.005
Iron	Balance	Balance	Balance

Table 2: Summary of the electron beam properties for each of the six welds along with the resulting weld depths and widths across the top surface of the plate.

Weld	Focus	Peak PD	FWHM	Diameter	Weld	Weld Width
	Setting	(W/mm ²)	(mm)	(mm)	Depth	(mm)
	(mA)	, , ,			(mm)	
1	762 (+32)	1500	0.49	0.98	0.98	1.53
2	760 (+30)	1550	0.51	0.97	1.03	1.52
3	760 (+30)	1510	0.51	0.98	1.11	1.56
4	759 (+29)	1480	0.54	1.00	1.14	1.55
5	759 (+29)	1445	0.52	1.01	1.00	1.53
6	759 (+29)	1470	0.51	0.99	0.99	1.51
Avg. / STD	759.8 / 1.2	1493 / 36.2	0.51 /.02	0.99 /.02	1.04 /.07	1.53 /.02

Table 3: Vickers microhardness measurements (50 gm load) made on the 21-6-9 base metal, weld HAZ, and weld fusion zone.

	Base Metal Hardness	HAZ Hardness	Weld Metal Hardness
Weld	Avg/STD (HV)	Avg/STD (HV)	Avg/STD (HV)
1	215.8 / 11.2	226.8 / 10.4	258.9 / 10.0
2	212.5 / 6.50	241.1 / 14.3	257.8 / 9.60
3	216.0 / 6.60	225.8 / 8.30	249.6 / 10.1
4	209.5 / 10.0	226.7 / 10.1	258.2 / 10.9
5	201.0 / 7.70	235.5 / 18.0	247.2 / 13.2
6	218.3 / 7.50	237.4 / 12.1	254.9 / 6.60
Avg. / STD	212.1 / 10.9	232.1 / 13.9	254.4 / 9.7
Number of Points	36	49	62

Table 4: Summary of the tensile test results on the base metal, milled cross-weld tensile samples, and full-thickness tensile samples. All samples tested at room temperature.

		1	ı	I	ı	1		1	
Sample Condition	Width	Thickness	Area	Gage Length	Xhd Speed	Young's Modulus	Elon.	Yield Strength	Ultimate Strength
	(in)	(in)	(in²)	(in)	(in/min)	(Msi)	(%)	(ksi)	(ksi)
Base Metal									
Mini	0.1009	0.0302	0.0031	0.225	0.02	29.0	71	50.0	103.1
Mini	0.101	0.0297	0.0030	0.225	0.02	28.6	80	50.2	104.4
Standard	0.2492	0.0303	0.0076	1.071	0.05	30.7	62	53.0	104.0
Standard	0.2491	0.0299	0.0075	1.0928	0.05	30.7	58	52.0	103.4
Standard	0.2491	0.0290	0.0072	1.0938	0.05	29.6	47	52.8	101.6
As Welded									
Mini	0.0998	0.0383	0.0038	0.1394	0.02	N/A*	24	67.0	102.3
Mini	0.0998	0.0355	0.0035	0.1381	0.02	N/A*	27	70.0	110.2
Mini	0.0998	0.0373	0.0037	0.107	0.02	N/A*	22	75.5	108.3
Standard	0.2488	0.0380	0.0095	1.081	0.05	N/A*	9.6	76.0	108.1
Standard	0.249	0.0358	0.0089	1.069	0.05	N/A*	9.5	76.3	107.2
Standard	0.2481	0.0370	0.0092	1.0638	0.05	N/A*	9.4	75.9	107.3
Welded/Milled									
Mini	0.1007	0.0299	0.0030	0.225	0.02	28.0	73	55.7	105.5
Mini	0.1007	0.0303	0.0031	0.225	0.02	28.6	69	55.5	105.8
Mini	0.1003	0.0303	0.0030	0.225	0.02	29.6	73	54.4	105.1
Standard	0.2492	0.0306	0.0076	1.0834	0.05	28.6	63	53.5	104.4
Standard	0.2493	0.0301	0.0075	1.0912	0.05	28.6	54	52.8	103.9
Standard	0.2492	0.0302	0.0075	1.0892	0.05	29.6	55	54.0	105.1
Voung's modulus not accurate due to cample handing in the as welded cross tensile samples									

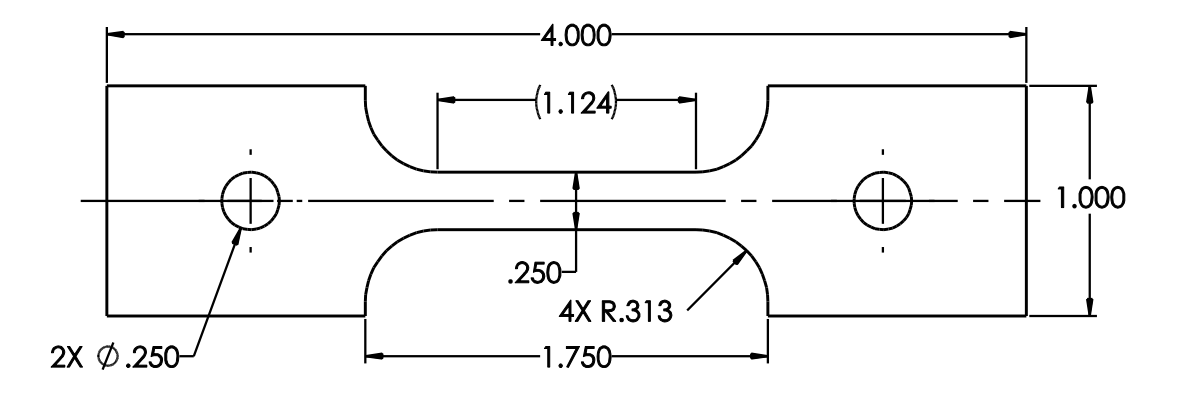
^{*}Young's modulus not accurate due to sample bending in the as-welded cross tensile samples.

Table 5: Recommended Steinberg-Guinan parameters for the 21-6-9 SS experimental weld metal and annealed base metal values under quasi-static strain rate conditions, compared to the published base metal value at high strain rates.

Steinberg-	Definition	Base Metal	Base Metal	Weld Metal
Guinan		Published Value	Experimental	Value
Parameter		[12]	Value	
		(high rate)	(quasi-static)	(quasi-static)
Yo	Yield Stress	0.0068 Mbar	0.0035 Mbar	0.0044 Mbar
		(680 MPa)	(350 MPa)	(440 MPa)
β	Hardening Coefficient	35	20	33
n	Hardening Exponent	0.23	0.5	0.375
Y _{max}	Saturation Stress	0.025 (2.5 GPa)	0.025 (2.5 GPa)	0.025 (2.5 GPa)

Table 6: Recommended Johnson-Cook strength parameters for the 21-6-9 SS weld metal and annealed base metal, under quasi-static strain rate conditions. ('B' updated Feb 2013).

Johnson- Cook	Definition	Base Metal Value	Weld Metal Value	
Parameter		(quasi-static)	(quasi-static)	
^	Effective Yield Stress	0.0055 Mbar	0.0078 Mbar	
A	at $\dot{\varepsilon}_{o}$ =1/s and T=RT	(550 MPa)	(780 MPa)	
В	Hardening	0.024 Mbar	0.024 Mbar	
Б	Coefficient	(2400 MPa)	(2400 MPa)	
n	Hardening	0.65	0.65	
	Exponent	0.05	0.03	
С	Strain Rate Coefficient	0.044	0.044	
m	Temperature Exponent	1.0	1.0	
T _{melt}	Melting Temperature	2380 K	2380 K	
T _{room}	Ambient Room Temperature	295 K	295 K	
$\dot{\mathcal{E}}_{O}$	Reference Strain Rate	1/s	1/s	



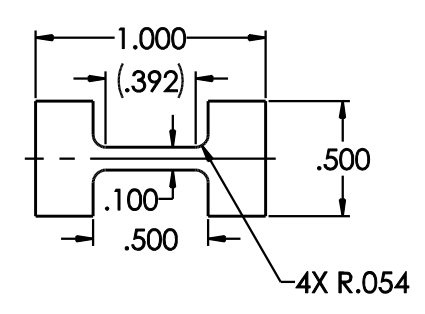


Figure 1: Drawings of the standard size (top) and mini (bottom) base metal tensile bars with dimensions in inches. Cross-weld samples would be prepared from two welded sheets with the weld running across the center of the gage length and perpendicular to the tensile bar axis.

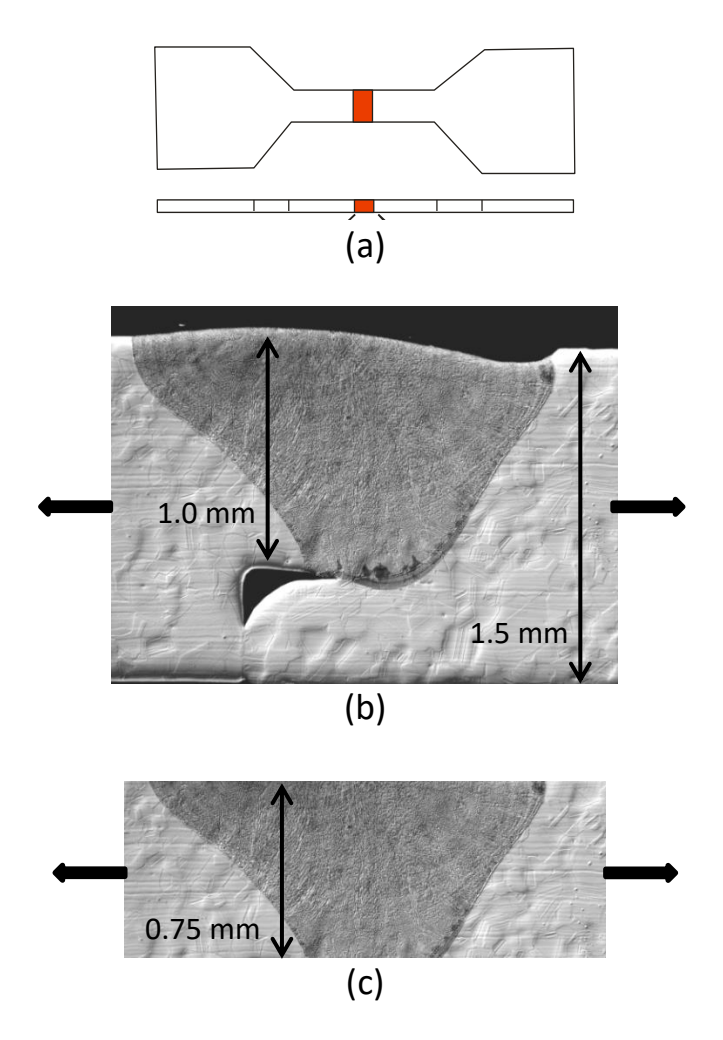


Figure 2: a) Illustration of the top and side views of cross-weld tensile bar, where the red shading indicates the weld location. b) micrograph of the full thickness type 1 weld coupon with step-joint related change in section thickness, c) cropped photo illustrating the cross section of the weld coupon after milling to remove the unwelded material below the step, the weld reinforcement, and the weld undercut. The horizontal arrows indicate the tensile axis direction relative to the weld.

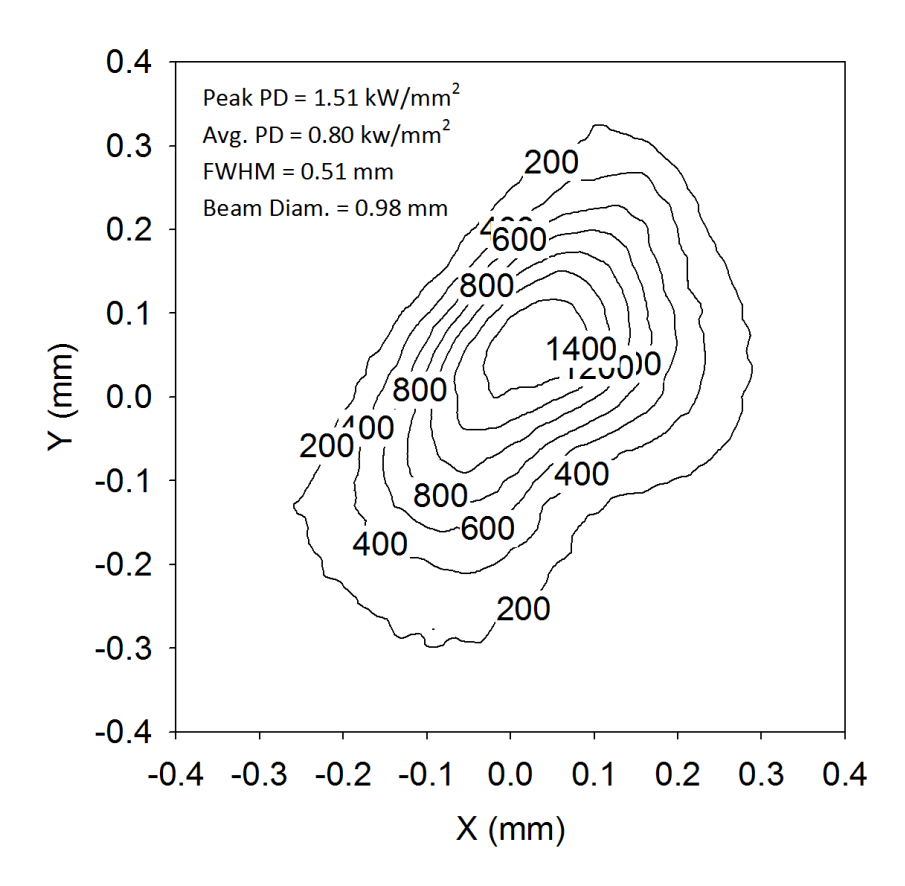


Figure 3: Power density distribution (W/mm²) and beam statistics for one of the electron beams used to make the welds, as measured by the EMFC diagnostic device.

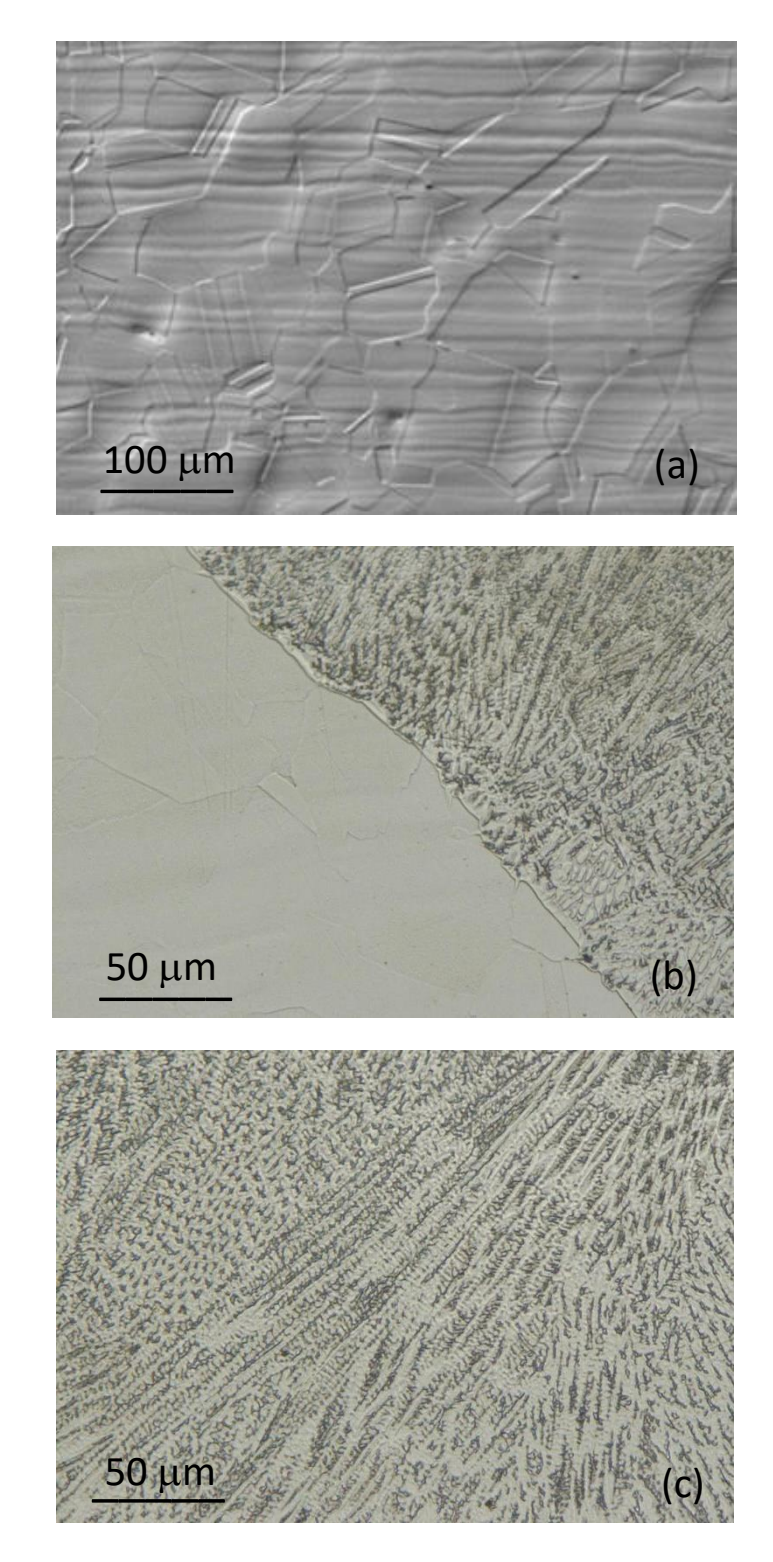


Figure 4: High magnification photomicrographs of: a) the base metal with a grain size of approximately 50 μ m, b) the fusion boundary of weld, and c) the central portion of the fusion zone showing the cellular/dendritic microstructure with a primary spacing of approximately 5 μ m.

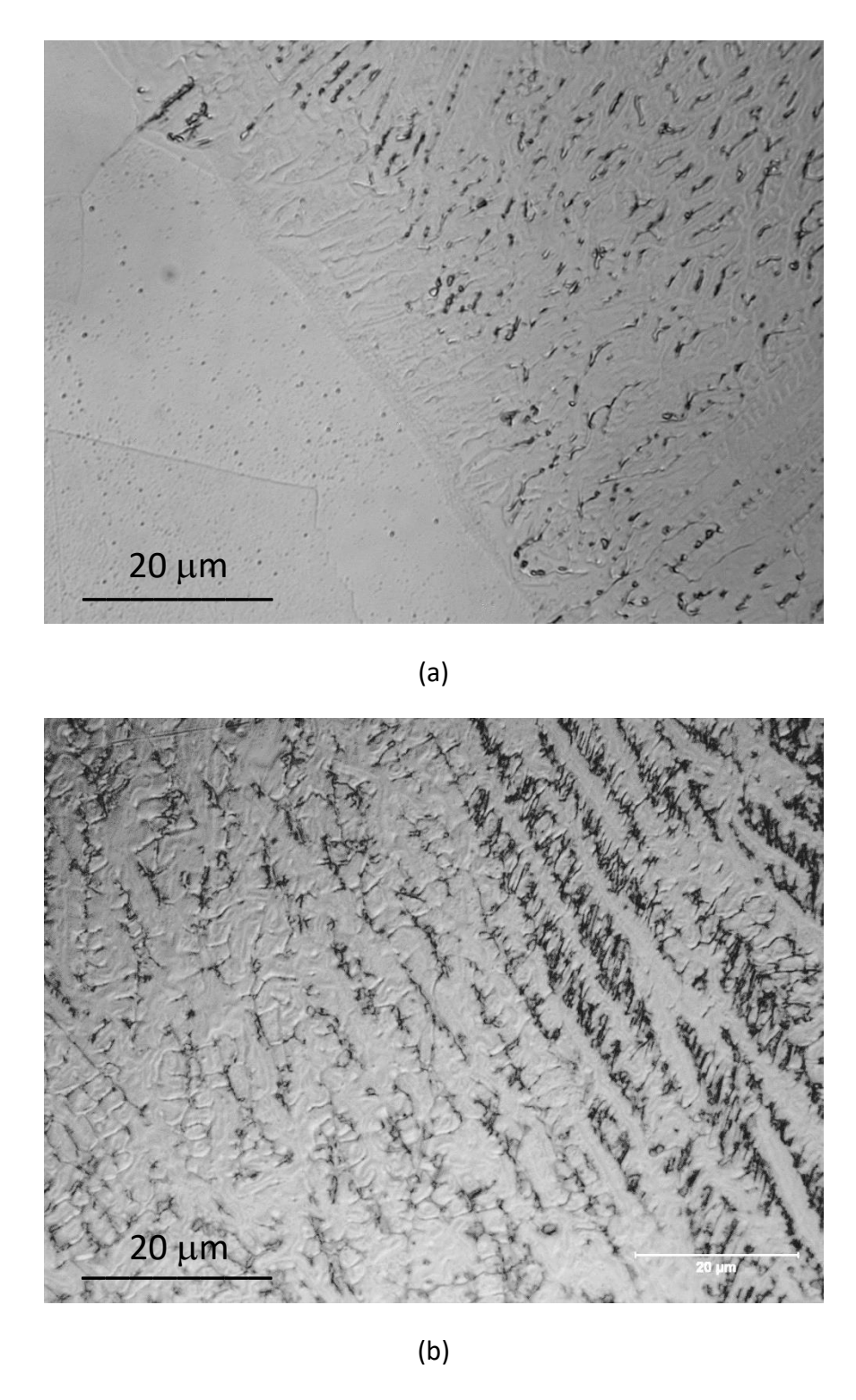
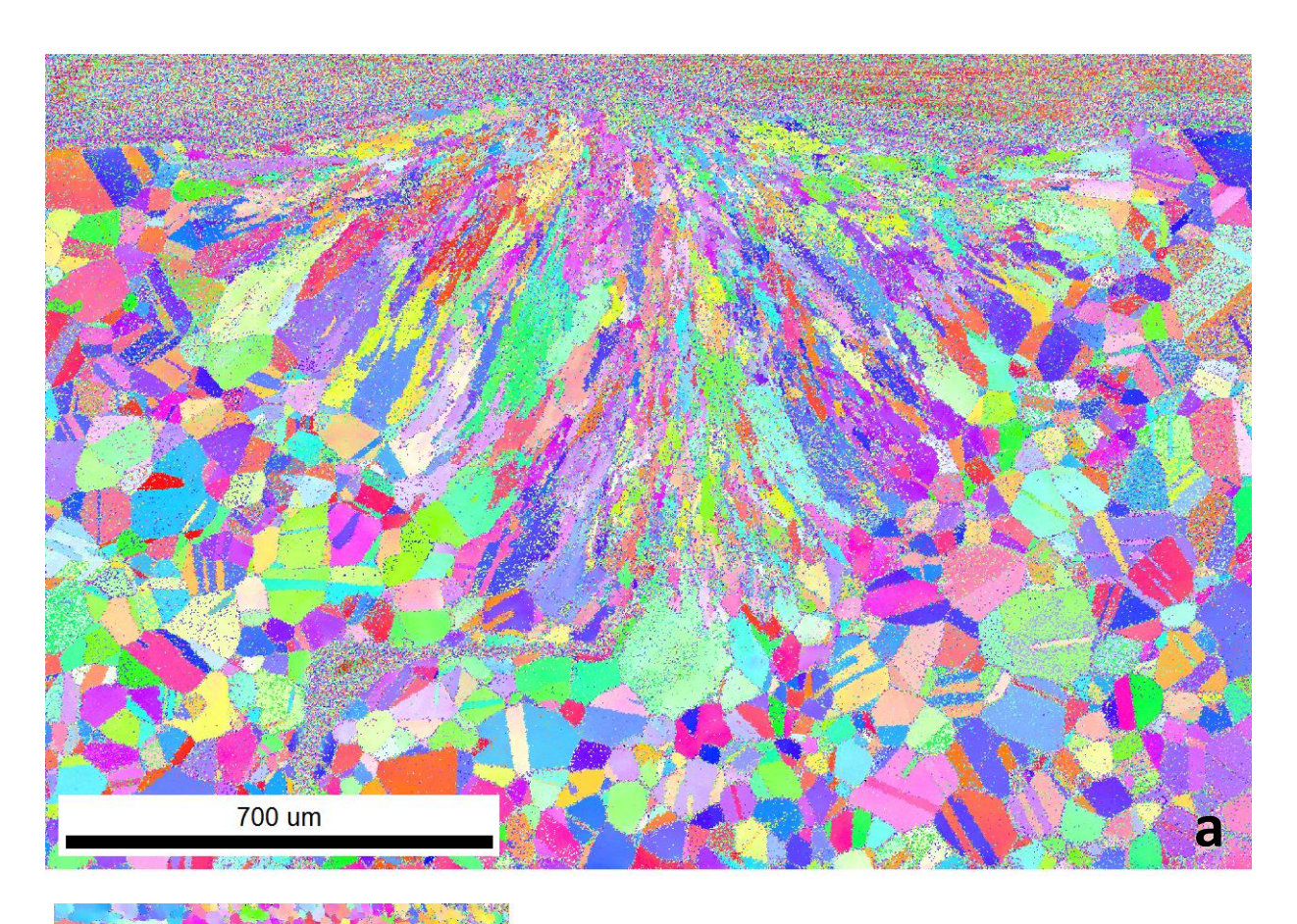


Figure 5: High magnification micrograph a) the fusion line of the weld, and b) the center section of the fusion zone. The dark etching phase is residual delta ferrite. Both photos shot at 1000x.







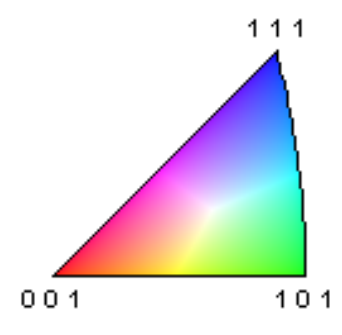


Figure 6: EBSD 001 inverse pole figure results showing grian orientatoin on a cross section of one of the welds. a) shows the entire weld and base metal grains with 2 micron step size, b) shows a zoomed in region of the weld fusion zone at 0.1 micron step size.

Mini Samples

Standard Samples

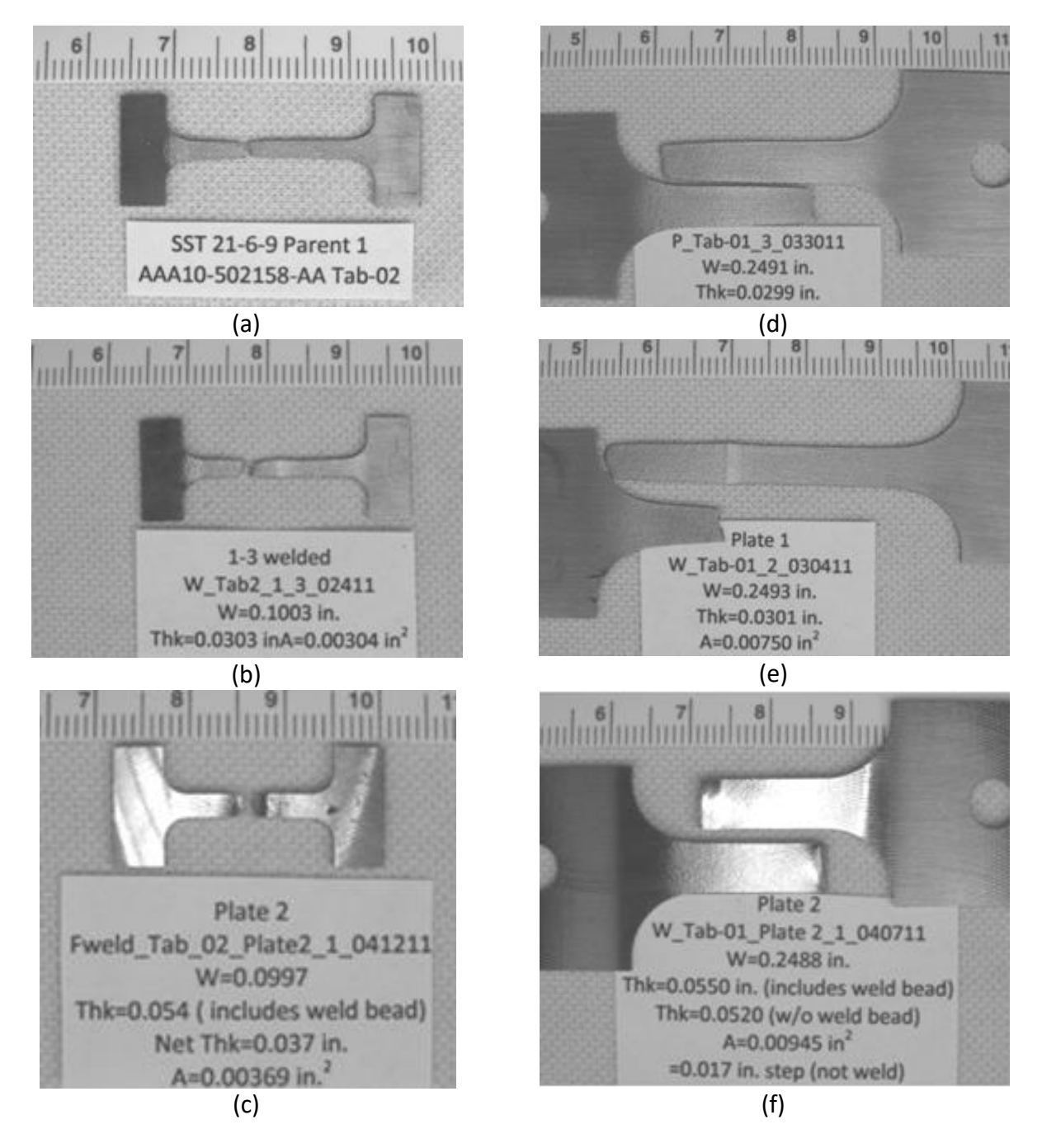


Figure 7: Photographs of representative tensile bars for each of the six different configurations.

(a) and (d) show base metal samples, (b) and (e) show milled weld samples, while (C) and (f) show as welded samples after tensile testing. The small divisions in the scale markers in the photographs are 1 mm increments.

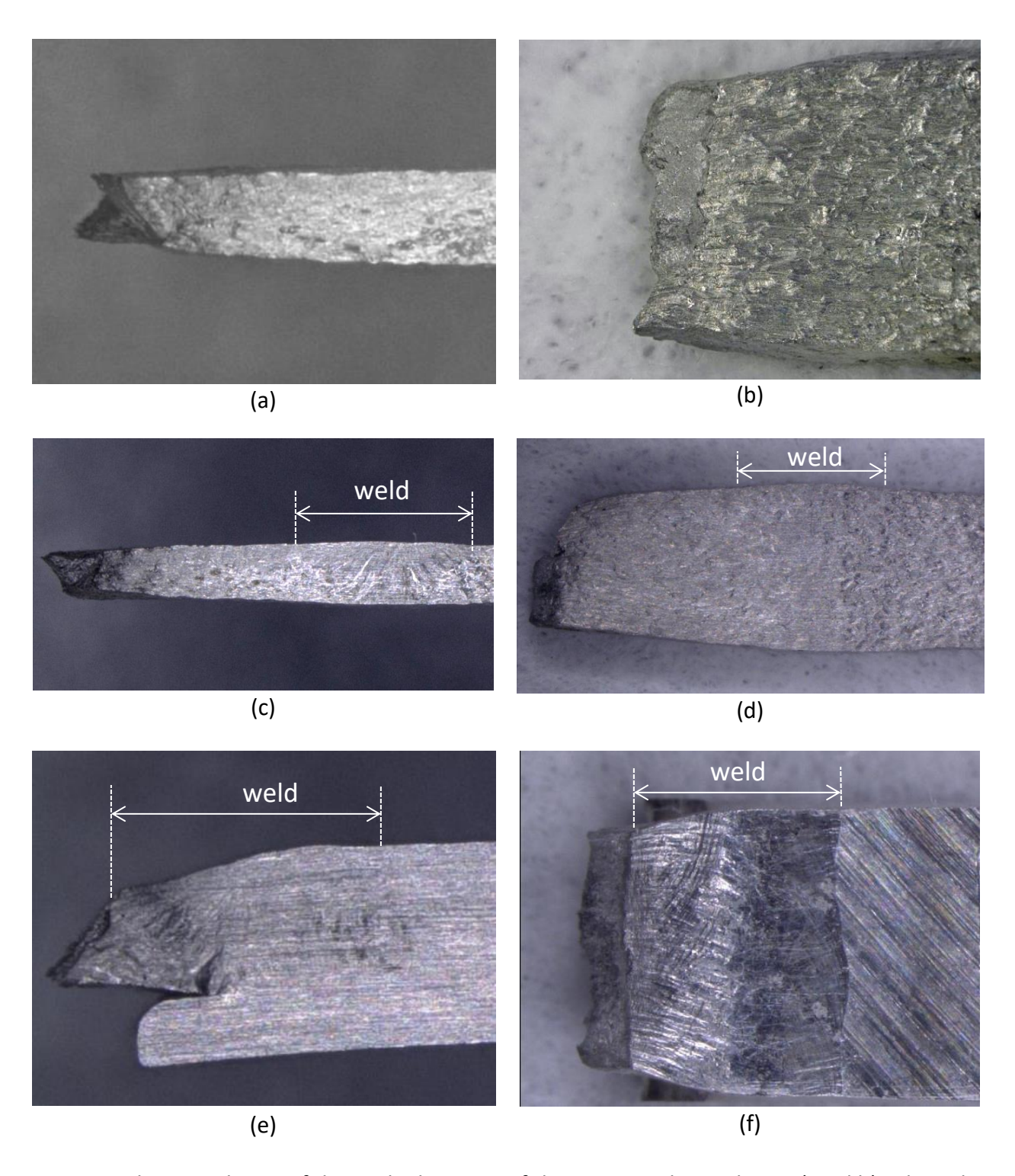


Figure 8: Close up photos of the necked regions of the mini tensile test bars: a) and b) side and top views of the base metal sample respectively; c) and d) side and top views of the milled cross-weld sample respectively; e) and f) side and top views of the full-thickness cross-weld sample respectively. Various magnifications; horizontal arrows indicate location of the welds.

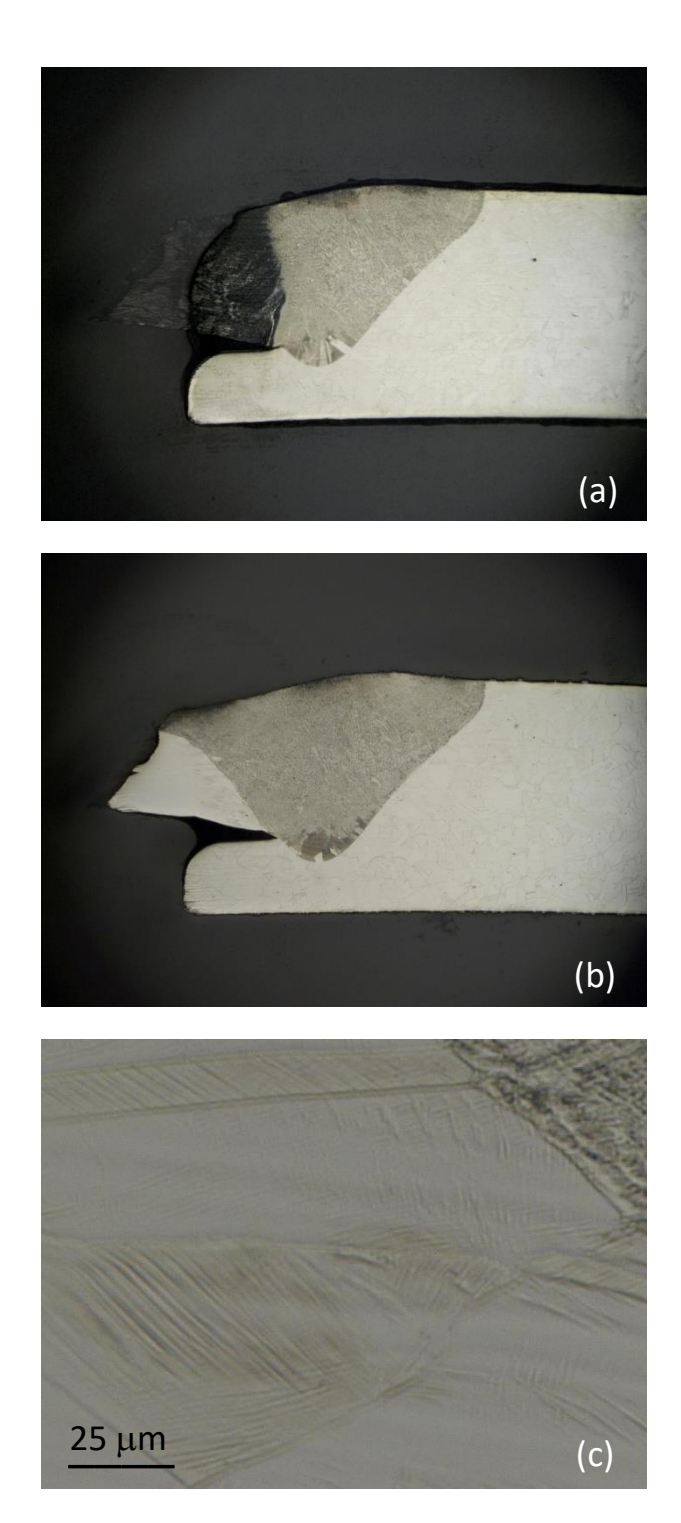


Figure 9: Full thickness mini sample after tensile testing. a) Sample after light polish of surface, showing deformation in the region directly above the unwelded portion of the step.
b) After lapping the sample to a depth ~1 mm below the surface to show necking and final failure location in the base metal. C) High magnification micrograph of the fusion line in the failed portion of the sample, showing deformation bands in the base metal.

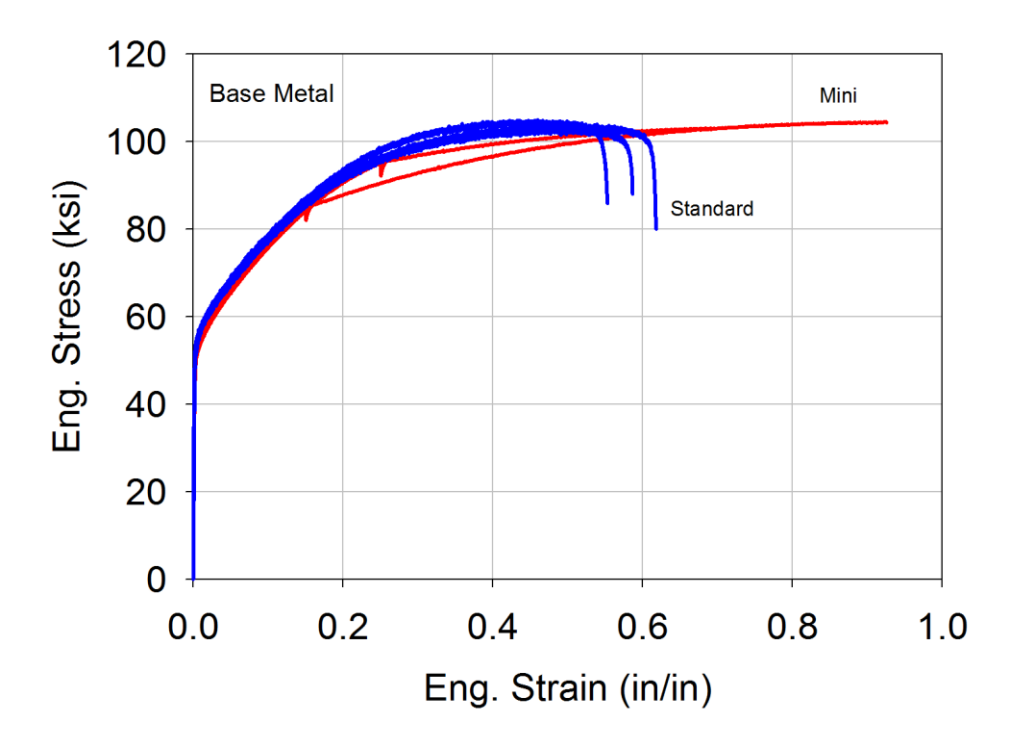


Figure 10: Base metal stress strain curves for the standard and mini tensile bars.

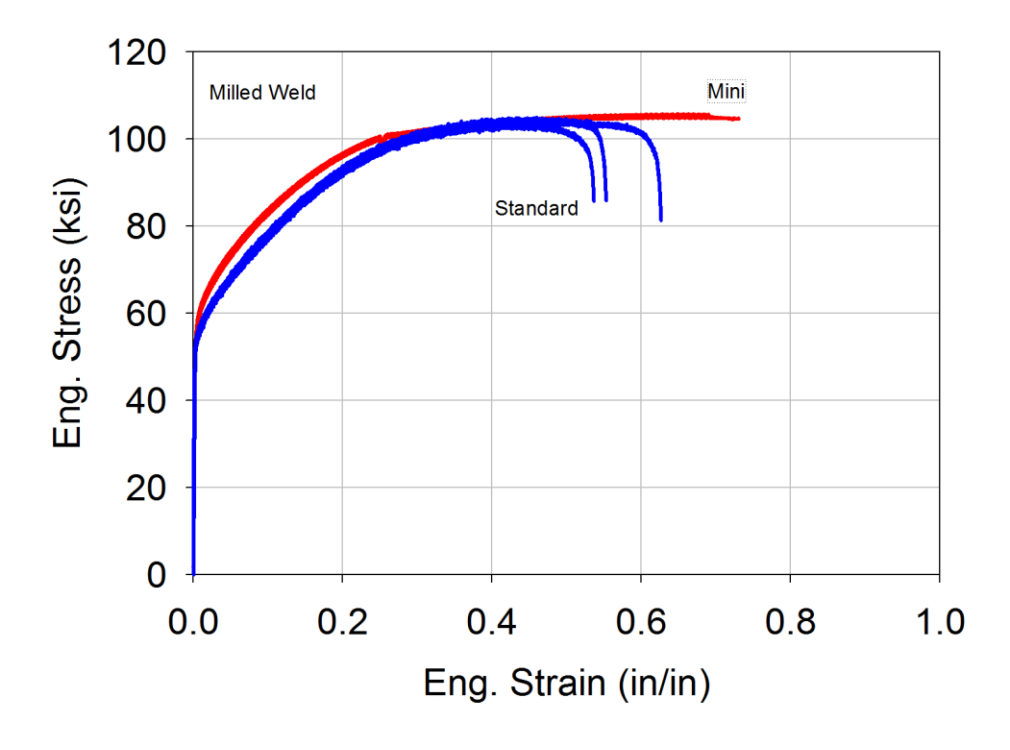
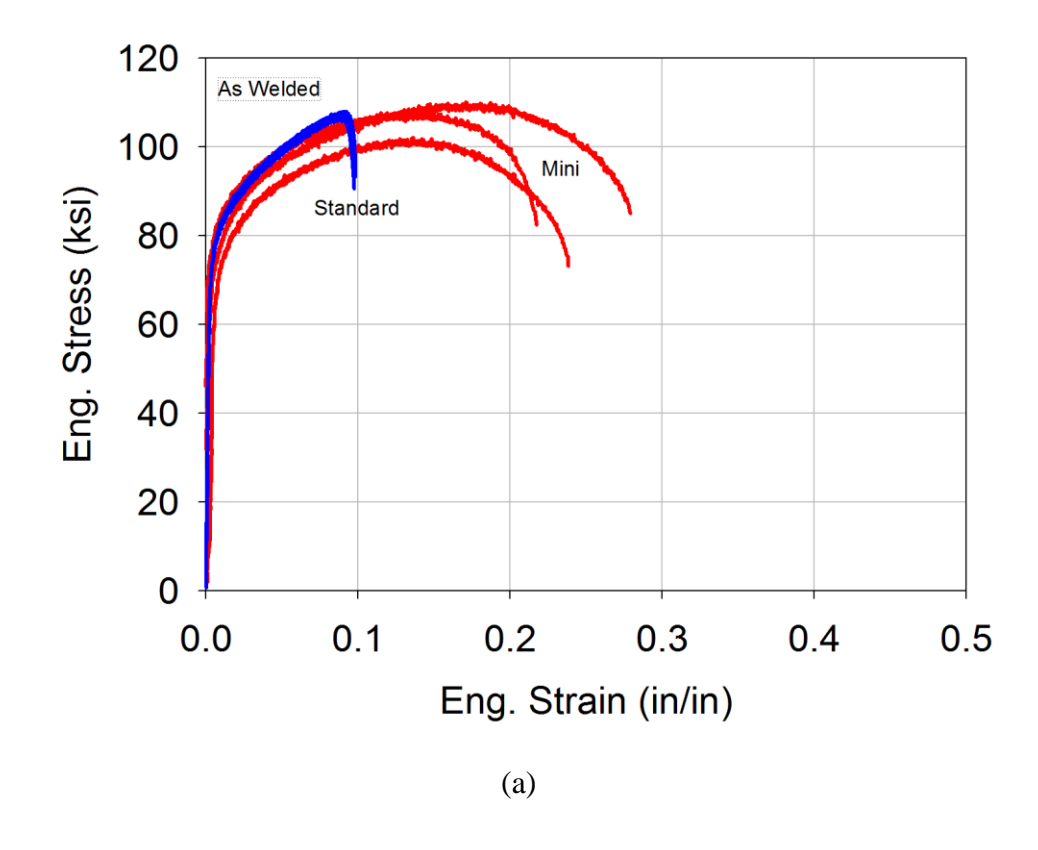


Figure 11: Milled cross-weld sample stress strain curves for the standard and mini tensile bars.



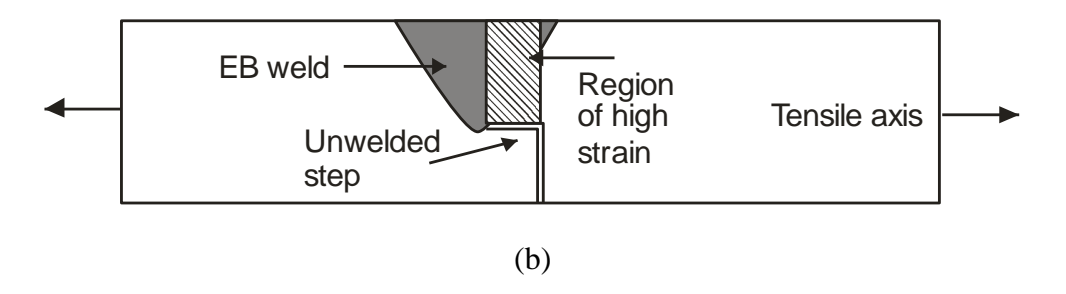


Figure 12: a) Full thickness, as welded, cross-weld sample stress strain curves for the standard and mini tensile bars. b) Schematic drawing of the as welded sample illustrating the high strain region directly above the unwelded portion of the step.

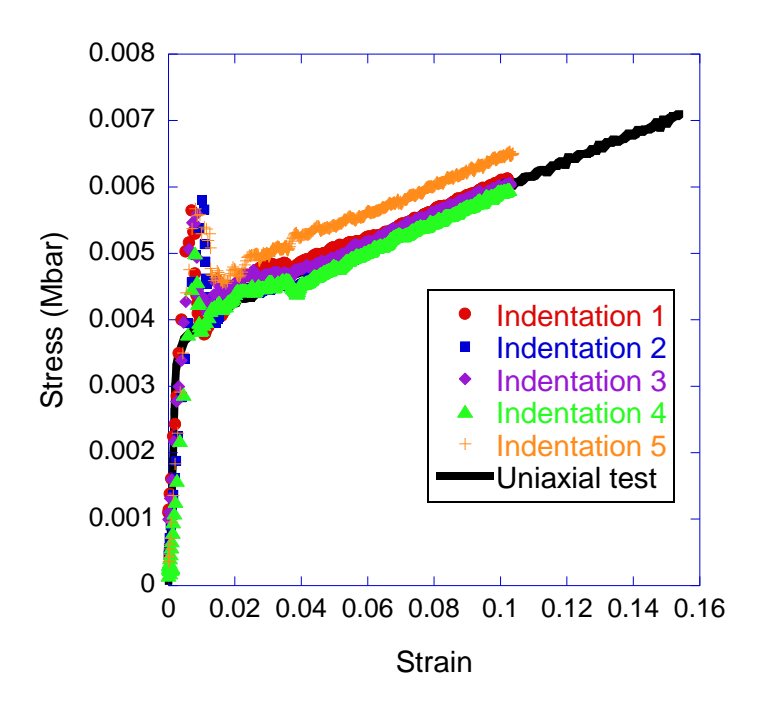


Figure 13: Stress-strain data from the 21-6-9 base metal. The stress-strain data from the indentation tests are compared to the uniaxial tests. A Tabor factor of 3.6 is used to match the data.

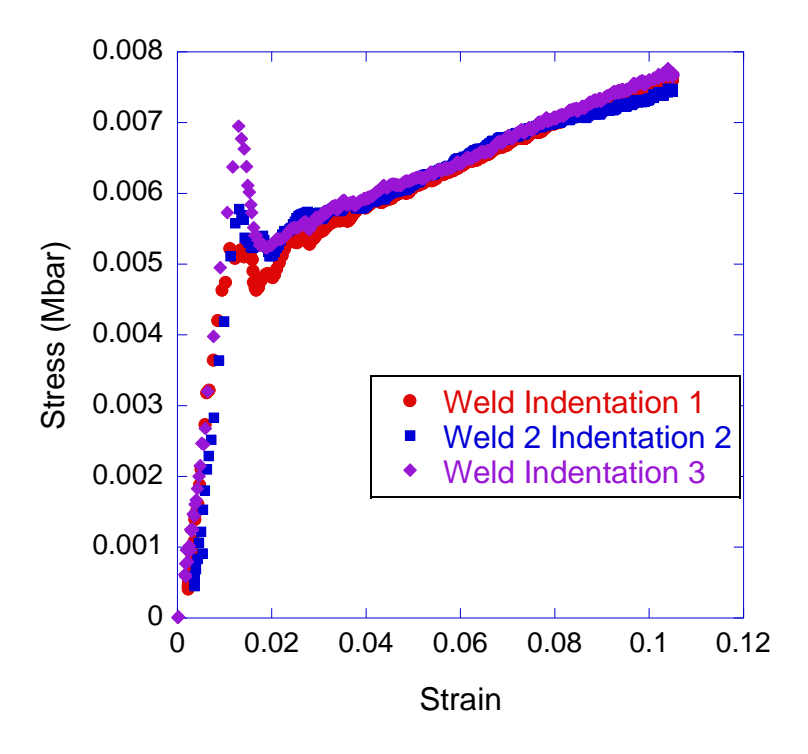


Figure 14: Stress-strain data from indentation tests for the 21-6-9 SS weld metal. The same Tabor factor of 3.6 is used.

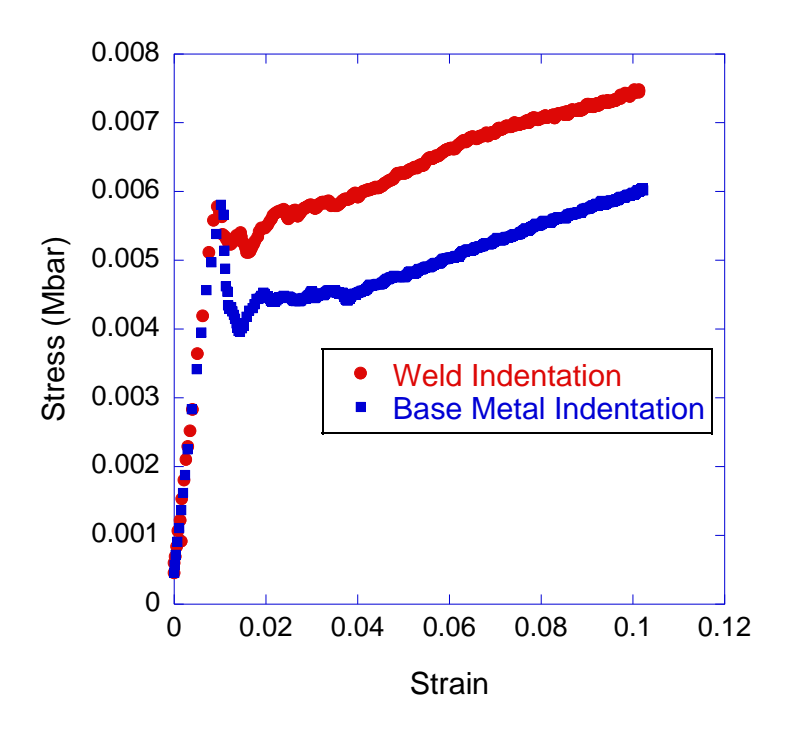


Figure 15: Comparison of stress-strain data from indentation tests for the 21-6-9 SS weld and base metal. The Tabor factor of 3.6 is used.

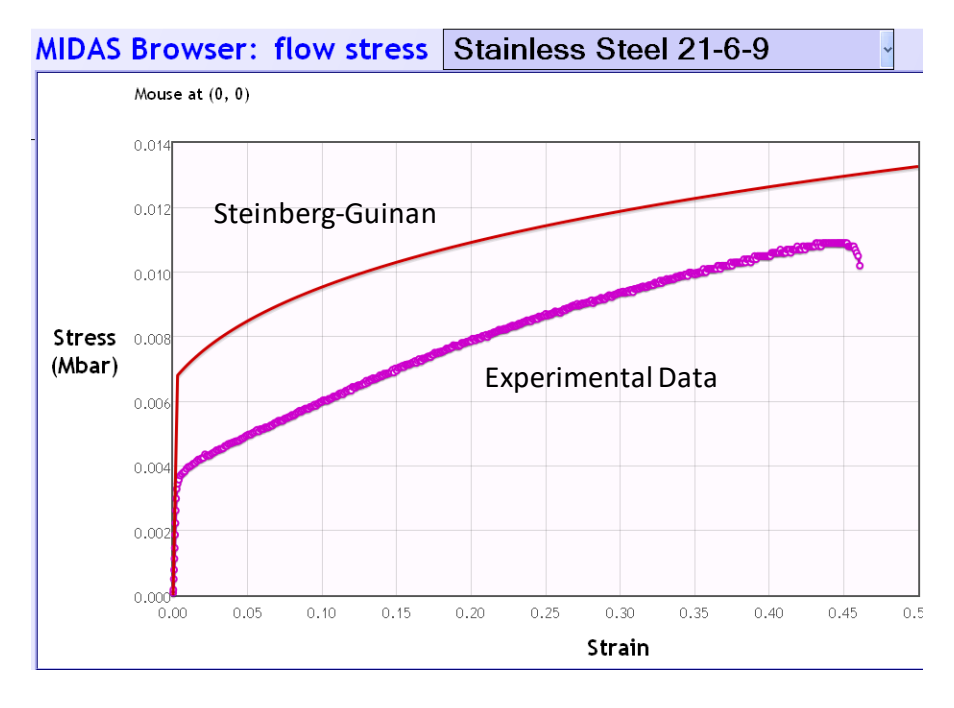


Figure 16: Comparison of the published Steinberg-Guinan parameters (optimized for high strain rates) to the experimental data of this study for annealed 21-6-9 SS base metal measured at quasi-static strain rates.

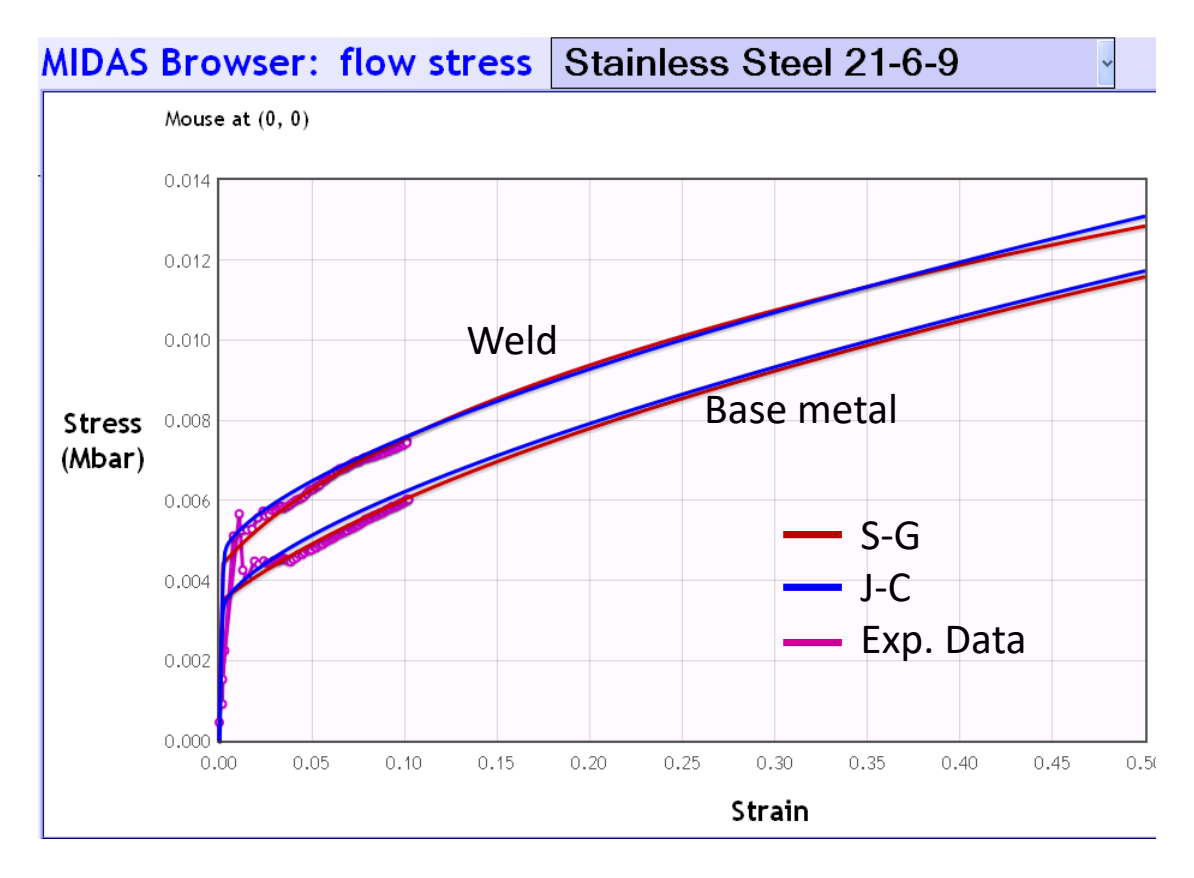


Figure 17: Steinberg-Guinan (S-G) and Johnson-Cook (J-C) stress-strain curve fits for the 21-6-9 SS base metal and weld metal using MIDAS to extrapolate the material behavior to larger strains. Both fits are superimposed over the spherical indentation experimental data.